Use of weather research and forecasting model outputs to obtain near-surface refractive index structure constant over the ocean

Chun Qing,[1,2] Xiaoqing Wu,[1,*] Xuebin Li,[1] Wenyue Zhu,[1] Chunhong Qiao,[1] Ruizhong Rao,[1] and Haipin Mei[1]

[1]*Key Laboratory of Atmospheric Composition and Optical Radiation, Anhui Institute of Optics and Fine Mechanics, Chinese Academy of Science, Hefei, Anhui 230031, China*
[2]*Science Island Branch of Graduate School, University of Science and Technology of China, Hefei, Anhui 230026, China*
[*]*xqwu@aiofm.ac.cn*

Abstract: The methods to obtain atmospheric refractive index structure constant (C_n^2) by instrument measurement are limited spatially and temporally and they are more difficult and expensive over the ocean. It is useful to forecast C_n^2 effectively from Weather Research and Forecasting Model (WRF) outputs. This paper introduces a method that WRF Model is used to forecast the routine meteorological parameters firstly, and then C_n^2 is calculated based on these parameters by the Bulk model from the Monin-Obukhov similarity theory (MOST) over the ocean near-surface. The corresponding C_n^2 values measured by the micro-thermometer which is placed on the ship are compared with the ones forecasted by WRF model to determine how this method performs. The result shows that the forecasted C_n^2 is consistent with the measured C_n^2 in trend and the order of magnitude as a whole, as well as the correlation coefficient is up to 77.57%. This method can forecast some essential aspects of C_n^2 and almost always captures the correct magnitude of C_n^2, which experiences fluctuations of two orders of magnitude. Thus, it seems to be a feasible and meaningful method that using WRF model to forecast near-surface C_n^2 value over the ocean.

OCIS codes: (010.1290) Atmospheric optics; (010.1330) Atmospheric turbulence; (030.4070) Modes; (010.3310) Laser beam transmission.

References and links

1. V. I. Tatarskii, *Wave Propagation in a Turbulent Medium* (McGraw-Hill, 1961).
2. D. L. Fried, G. E. Mevers, and M. P. Keister, "Measurements of laser beam scintillation in the atmosphere," J. Opt. Soc. Am. **57**, 787-797 (1967).
3. T. Chiba,"Spot dancing of the laser beam propagated through the turbulent atmosphere," Appl. Opt. **10**, 2456-2461 (1971).
4. M. Sarazin and F. Roddier, "The ESO differential image motion monitor," Astronomy Astrophys. **227**, 294-300 (1990).
5. R. Avila, J. Vernin, and E. Masciadri,"Whole atmospheric-turbulence profiling with generalized scidar," Appl. Opt. **36**(30), 7898-7905 (1997).
6. V. Kornilov, A. Tokovinin, N. Shatsky, O. Voziakova, S. Potanin, and B. Safonov, "Combined MASS-DIMM instruments for atmospheric turbulence studies," MNRAS **382**, 1268-1278 (2007).

#260823 Received 8 Mar 2016; revised 13 May 2016; accepted 31 May 2016; published 8 Jun 2016

7. E. Masciadri, J.Vernin, and P. Bougeault, "3D mapping of optical turbulence using an atmospheric numerical model. I. A useful tool for the ground-based astronomy," Astronomy Astrophys. **137**, 185-202 (1999).
8. E. Masciadri, J.Vernin, and P. Bougeault, "3D mapping of optical turbulence using an atmospheric numerical model. II. First results at Cerro Paranal," Astronomy Astrophys. **137**, 203-216 (1999).
9. E. Masciadri, J. Vernin, and P. Jabouille, "3D numerical simulations of optical turbulence at the Roque de Los Muchachos Observatory using the atmospherical model Meso-Nh," Astronomy Astrophys. **365**, 699-708 (2001).
10. E. Masciadri, and P. Jabouille, "Improvements in the optical turbulence parameterization for 3D simulations in a region around a telescope," Astronomy Astrophys. **376**, 727-734 (2001).
11. E. Masciadri, R. Avila, and L. J. Sanchez, "Statistic reliability of the Meso-Nh atmospherical model for 3D C_n^2 simulations," RMxAA **40**, 3-14 (2004).
12. E. Masciadri, and S. Egner, "First seasonal study of optical turbulence with an atmospheric model," Pub. Astronomical Soc. Pac. **118**, 1604-1619 (2006).
13. S. Hagelin, E. Masciadri, and F. Lascaux, "Optical turbulence simulations at Mt Graham using the Meso-NH model," MNRAS **412**, 2695-2706 (2011).
14. E. Masciadri, and F. Lascaux, "MOSE: operational forecast optical turbulence and atmospheric parameters at European Southern Observatory ground-based sites - I. Overview and vertical stratification of atmospheric parameters at 0-20 km.," MNRAS **436**(3), 1968-1985 (2013).
15. F. Lascaux, E. Masciadri, S. Hagelin, and J. Stoesz, "Mesoscale optical turbulence simulations at Dome C," MNRAS **398**, 1093-1104 (2009).
16. F. Lascaux, E. Masciadri, and S. Hagelin, "Mesoscale optical turbulence simulations above Dome C, Dome A and South Pole," MNRAS **411**, 693-704 (2011).
17. T. Cherubini, S. Businger, R. Lyman, and M. Chun, "Modeling optical turbulence and seeing over Mauna Kea," J. Appl. Meteorol. Chem. **47**, 1140-1155 (2008).
18. T. Cherubini, S. Businger, R. Lyman, and M. Chun, "Modeling turbulence and seeing over Mauna Kea: Verification and Algorithm Refinement," J. Appl. Meteorol. Chem. **47**, 3033-3043 (2008).
19. T. Cherubini, S. Businger, "An operational perspective for modeling optical turbulence," in *Seeing Clearly: The Impact of Atmospheric Turbulence on the Propagation of Extraterrestrial Radiation*, S. Businger and T. Cherubini, eds. (VBW Publishing, 2011).
20. T. Cherubini, S. Businger, "Another look at the refractive index function," J. Appl. Meteorol. Chem. **52**, 498-506 (2012).
21. C. Giordano, J. Vernin, H. Vazquez Ramio, C. Munoz-Tunon, A. M. Varela and H. Trinquet, "Atmospheric and seeing forecast: WRF model validation with in situ measurements at ORM," MNRAS **430**, 3102-3111 (2013).
22. C. Qing, X. Wu, X. Li, W. Zhu, R. Rao, and H. Mei, "Estimation of atmospheric optical turbulence profile by WRF model at Gaomeigu," Chinese J. Lasers **42**(9), 0913001 (2015).
23. S. Cheinet, A. Beljaars, K. Weiss-Wrana, and Y. Hurt, " The use of weather forecasts to characterise near-surface optical turbulence," Boundary-Layer Meteor **138**, 453-473 (2011).
24. J. C. Wyngaard, Y. Izumi, and J. S. A. Collins, "Behavior of the refractive-index-structure parameter near the ground," J. Opt. Soc. Am. **61**(12),1646-1650 (1971).
25. C. A. Friehe, J. C. La Rue, and F. H. Champagne, C. H. Gibson, and G. F. Dreyer, "Effects of temperature and humidity fluctuations on the optical refractive index in the marine boundary layer," J. Opt. Soc. Am. **65**(12), 1502-1511 (1975).
26. C. A. Friehe, "Estimation of the refractive-index temperature structure parameter over the ocean," Appl. Opt. **16**(2), 334-340 (1977).
27. K. L. Davidson, G. E. Schacher, C. W. Fairall, and A. K. Goroch, "Verification of the bulk method for calculating overwater optical turbulence," Appl. Opt. **20**(17), 2919-2924 (1981).
28. P. A. Frederickson, K. L. Davidson, C. R. Zeisse, and C. S. Bendall, "Estimating the refractive index structure parameters (C_n^2) over the ocean using bulk methods," J. Appl. Meteorol. **39**, 1770-1783 (2000).
29. P. A. Frederickson, S. Hammel, and D. Tsintikidis, "Measurements and modeling of optical turbulence in a maritime environment," Proc. SPIE **6303**, 630307 (2006).
30. X. Wu, X. Zhu, H. Huang, and S. Hu, "Optical turbulence of atmospheric surface layer estimated based on the Monin-Obukhov similarity theory," Acta Opt. Sin **32**(7), 0701004 (2012).
31. W. C. Skamarock, J. B. Klemp, J. Dudhia, D. O. Gill, D. M. Barker, M. G. Duda, X. Huang, W. Wang, and J. G. Powers, "A Description of the Advanced Research WRF Version 3," (NCAR Technical Note, NCAR/TN-475+STR, 2008).
32. E. L. Andreas, "Estimating C_n^2 over snow and ice from meteorological data," J. Opt. Soc. Am. 5**A**, 481-495 (1988).
33. C. W. Fairall, and S. E. Larsen, "Inertial dissipation methods and turbulent fluxes at the airocean interface," Boundary-Layer Meteor **34**, 287-301 (1986).
34. E. L. Andreas, R. J. Hill, J. R. Gosz, D. I. Moore, W. D. Otto, and A. D. Sarma, "Statistics of surface-layer turbulence over terrain with metre-scale heterogeneity," Boundary-Layer Meteor **86**, 379-408 (1998).
35. C. W. Fairall, G. E. Schacher, and K. L. Davidson, "Measurements of the humidity structure function parameters, C_q^2 and C_{Tq} over the ocean," Boundary-Layer Meteor **19**, 81-92 (1980).

#260823 Received 8 Mar 2016; revised 13 May 2016; accepted 31 May 2016; published 8 Jun 2016

36. C. W. Fairall, E. F. Bradley, D. P. Rogers, J. B. Edson, and G. S. Young, "Bulk parameterization of airsea fluxes for tropical oceanglobal atmosphere coupledocean atmosphere response experiment," J. Geo. Res **101**(C2), 3747-3764 (1996).
37. J. Wu, "Wind-stress coefficients over sea surface near neutral conditions-A revisit," J. Phys. Oceanogr. **10**, 727-740(1980).
38. W. T. Liu, K. B. Katsaros, and J. A. Businger, "Bulk parameterization of airsea exchanges of heat and water vapor including the molecular constraints at the interface," J. Atmos. Sci **36**, 1722-1735 (1979).
39. C. A. Paulson, "The mathematical representation of wind speed and temperature profiles in the unstable atmospheric surface layer," J. Appl. Meteorol. **9**, 857-861 (1970).
40. A. C. M. Beljaars and A. A. M. Holtslag, "Flux parameterization over land surfaces for atmospheric models," J. Appl. Meteorol. **30**, 327-341 (1991).
41. E. L. Andreas and A. P. Makshtas, "Energy exchange over Antarctic seaice in the spring," J. Geo. Res. **90**, 7199-7212 (1985).
42. A. M. Obukhov, "Structure of the temperature field in a turbulent flow," Ser Geograf. Geofiz. **13**, 58-69 (1949).
43. J. B. Edson, C. W. Fairall, P. G. Mestayer, and S. E. Larsen, "A study of the inertial-dissipation method for computing air-sea fluxes," J. Geo. Res. **96**, 10689-10711 (1991).
44. L. Mahrt, "Stratified atmospheric boundary layers," Boundary-Layer Meteor. **90**, 375-396 (1999).

1. Introduction

The electromagnetic waves propagating through the atmosphere changes as it encounters the inhomogeneities of refractive index caused by the atmospheric turbulence, which degrades the image quality of the photoelectric system dramatically [1-3]. Therefore, the knowledge of C_n^2 is essential to evaluate the performance of photoelectric system. The intensity of the atmospheric turbulence is usually described by refractive index structure constant (C_n^2, $m^{-2/3}$), and there are a variety of methods to measure it [4-6]. As almost all of methods using the instruments to obtain C_n^2 are limited in spatial-temporal domain, researchers propose a way to forecast C_n^2 from Numerical Weather Prediction (NWP) model outputs. In previous years, some representative studies have been carried out to forecast the parameters of atmospheric turbulence with Mesoscale Non-hydrostatic (Meso-Nh) model. Specially, Masciadri's group devotes themself to simulate optical turbulence with numerical model: The ability of Meso-Nh model to reproduce a correct spatial distribution of C_n^2 is supported by a comparison between Scidar measurements and simulations above Cerro Paranal (Chile) [7,8]. However, a set of 3D C_n^2 simulation which is provided by Meso-NH model shows that the horizontal distribution of the C_n^2 is not necessarily uniform, especially in the first 10 km above the ground [9]. Soon afterwards, a new calibration technique for the optical turbulence parameterization is proposed in order to reduce some systematic errors at astronomical site of Roque de los Muchachos (Canary Islands) [10]. Apply this calibration technique to a sample of 10 nights of the San Pedro Martir site testing campaign (Mexico), and the result shows that the dispersion between measurements and simulations is comparable to that obtained between different instruments measurement ($\leq$30%) [11-12]. Furthermore, a subsample of the C_n^2 profiles obtained with a generalized scidar from 41 nights is used for calibrating and quantifying the Meso-NH model's ability to reconstruct the optical turbulence above Mt Graham (Arizona, USA), site of the large binocular telescope, and the result shows a good ability in reconstructing the shape of the vertical distribution of C_n^2 as well as the seeing (ε), the isoplanatic angle (θ_0) and the wavefront coherence time (τ_0) [13]. On the one hand, the study employs a wide variety of measurements obtained with different instruments running simultaneously to constrain and validate the model at European Southern Observatory ground-based sites. Results obtained are very promising showing that the numerical simulation technique is already mature for an operational implementation in present and forthcoming observatories [14]. On the other hand, the ability of the Meso-Nh model to discriminate different types of optical turbulence behavior has been investigated above Dome C, Dome A and South Pole, and it is evident that three sites have different characteristics in view of the seeing and the surface-layer thickness [15,16]. Along with Cherubini's group work:

#260823 Received 8 Mar 2016; revised 13 May 2016; accepted 31 May 2016; published 8 Jun 2016

The two papers [17,18] present the problem of modeling seeing using the fifth-generation Pennsylvania State University-National Center for Atmospheric Research Mesoscale Model (MM5) model and the preliminary results from a validation study. Furthermore, the papers [19,20] explains how the system evolved into an operational prediction system where the C_n^2 or seeing (ε) algorithm is implemented within WRF model at the Mauna Kea Weather Center (MKWC), is operationally used at MKWC for prediction of both weather and optical turbulence, referring to website http://mkwc.ifa.hawaii.edu/models/index.cgi?model=wrf-hi. In addition, the validation of using WRF model to forecast atmospheric turbulence parameters has been performed above Observatory del Roque de Los Muchachos site and Gaomeigu Observatory (China). The result shows that this method is sturdy enough to be applied to potential astronomical sites where no instruments are available [21,22]. Besides, the method of using European Center for Medium Range Weather Forecasts (ECMWF) model products to calculate near-surface optical turbulence is evaluated against scintillometry measurements at climatologically distinct sites in western Europe, and the results show that the model can forecast some essential aspects of near-surface C_n^2 [23].

To our knowledge, using WRF model to forecast near-surface C_n^2 over the ocean is seldom reported. The Bulk model which is based on MOST provides a theoretical basis to calculate near-surface C_n^2 from routine meteorological parameters over the ocean [24-26]. The verification of the Bulk model for calculating C_n^2 overwater has been performed yet [27-30]. However, the instrument application is limited in lots of environment, such as the ocean surface as well as the complexity underlying surface. To mitigate the above limitation, in this study, we introduce a method of forecasting C_n^2 from routine meteorological parameters which are forecasted by WRF model coupled with Bulk model over the ocean near-surface. The C_n^2 values measured by the micro-thermometer which is placed on the ship that drops anchor close to the center grid of simulation domain (17.5°N, 109.5°E) used for a comparison.

In Section 2, we give a description of WRF model. In Section 3, we show the theoretical background of estimating C_n^2. In Section 4, we briefly describe the principle of the micro-thermometer. In Section 5, we compare the diurnal feature of C_n^2 between forecast and measurement. In Section 6, we discuss the possible causes of the deviation and the improvements. Finally, the conclusion of this study is drawn in Section 7.

2. WRF model configuration

WRF model is a mesoscale numerical weather prediction model used for both professional forecasting and atmospheric research. It is developed by the National Center of Environment Prediction (NCEP) of the United States and the National Center of Atmospheric Research (NCAR) of the United States. Details of governing equations, transformations and grid adaptation are given in Modeling System User's Guide, referring to http://www2.mmm.ucar.edu/wrf/users/docs/user_guide_V3/contents.html. In this study, WRF is initialized with the Global Forecast System (GFS) data that has a horizontal resolution of $1^\circ \times 1^\circ$ (in longitude and latitude), downloaded from the NCEP website http://www.ncep.noaa.gov/. The basic simulation parameters setting are listed in Table 1, and the simulation area is shown in Fig. 1.

WRF model exports a large number of routine meteorological parameters (such as temperature, absolute humidity, pressure, wind speed, etc.) which depend upon the physical schemes that have been chosen for the simulation. The main physical schemes used for the simulation are listed in Table 2, and the detailed physical schemes are explained as follows [31]:

(1) The micro-physics process uses the WRF Single-Moment 3 class (WSM-3) scheme which is suitable for medium-scale grid dimension, and contains three kinds of water materials: water vapor, cloud water or cloud ice, rainwater or snow.

#260823 Received 8 Mar 2016; revised 13 May 2016; accepted 31 May 2016; published 8 Jun 2016

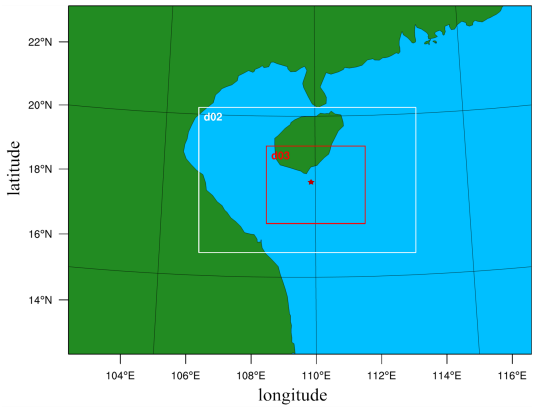

Fig. 1. Simulation area (The South Sea of China), the red solid star represents the center grid of simulation domain (17.5°N, 109.5°E).

Table 1. The basic parameter setting

Parameter	Setting
Center latitude and longitude	17.5°N, 109.5°E
Horizontal grid numbers (Domain 1, Domain 2, Domain 3)	64 × 48, 90 × 60, 123 × 96
Horizontal grid resolution (Domain 1, Domain 2, Domain 3)	27 km, 9 km, 3 km
Vertical layers	40
Output time interval	30 minutes
Map projection	Lambert
Initialized field data	GFS

(2) The Rapid Radiative Transfer Model (RRTM) scheme is used for the longwave radiation. The longwave process is caused by water vapor, ozone, carbon dioxide and other gases, as well as by the optical depth of cloud.

(3) The shortwave radiation uses the Goddard scheme which is suitable for cloud-resolution models, and contains the effect of graupel.

(4) The planetary boundary layer uses the Yonsei University (YSU) scheme which is suitable for simulating over the ocean, and adds the process of dealing with entrainment at the top of planetary boundary layer.

(5) The surface layer uses the Monin-Obukhov scheme which is based on the Monin-Obukhov theory.

(6) The cumulus parameterization uses the Kain-Fritsch scheme which consists of a cloud model concerning the water vapor lifting and subsidence, with the phenomena, such as, entrainment, detrainment, air-current ascension and subsidence covered.

3. Theoretical background

3.1. *The atmospheric refractive index structure constant (C_n^2)*

For visible and near-infrared wavelength (λ), the atmospheric refractive index fluctuation is mainly caused by temperature fluctuation. The refractive index for air (n) can be defined as follows [32]

$$n = 1 + 10^{-6}\left\{m_1(\lambda)\frac{P}{T}[m_2(\lambda) - m_1(\lambda)]\frac{qP}{T\varepsilon\gamma}\right\}, \quad (1)$$

#260823 Received 8 Mar 2016; revised 13 May 2016; accepted 31 May 2016; published 8 Jun 2016

Table 2. The main physical scheme setting

Physical scheme	Option
Micro-physics process	WRF Single-Moment 3 class
Longwave radiation	Rapid Radiative Transfer Model
Shortwave radiation	Goddard
Surface layer	Monin-Obukhov
Planetary boundary layer	YSU
Cumulus parameterization	Kain-Fritsch

where P is the atmospheric pressure (hPa), T is the absolute temperature (K), q is the absolute humidity (g/kg), ε = 0.622, and $\gamma = 1 + 0.61q$. The functions $m_1(\lambda)$ and $m_2(\lambda)$ are given by

$$m_1(\lambda) = 23.7134 + \frac{6839.397}{130 - \lambda^{-2}} + \frac{45.473}{38.9 - \lambda^{-2}}, \tag{2a}$$

$$m_2(\lambda) = 64.8731 + 0.5850\ 58\lambda^{-2} - 0.007\ 1150\lambda^{-4} + 0.000\ 8851\lambda^{-6}, \tag{2b}$$

in which λ is in micrometers. For the wavelength of interest in this study, λ = 0.55 μm , $m_1(\lambda)$ = 79.0 and $m_2(\lambda)$ = 66.7.

Because pressure fluctuations are very small, assuming pressure fluctuations are negligible [32]. The atmospheric refractive index fluctuation (n') can be expressed as

$$n' = A(\lambda, P, T, q)T' + B(\lambda, P, T, q)q', \tag{3}$$

where the coefficients A and B are defined as

$$A = \frac{\partial n}{\partial T} = 10^{-6}\frac{P}{T^2}\left\{m_1(\lambda) + [m_2(\lambda) - m_1(\lambda)]\frac{q}{\varepsilon\gamma}\right\}, \tag{4a}$$

$$B = \frac{\partial n}{\partial q} = 10^{-6}[m_2(\lambda) - m_1(\lambda)]\frac{P}{T\varepsilon\gamma^2}. \tag{4b}$$

For Kolmogorov turbulence, the atmospheric refractive index structure constant in the inertial-subrange is defined as

$$C_n^2 = \frac{\langle[n(\vec{x}) - n(\vec{x}+\vec{r})]^2\rangle}{r^{2/3}}, \quad l_0 \ll r \ll L_0, \tag{5}$$

where C_n^2 is called atmospheric refractive index structure constant, $\vec{x}$ and $\vec{r}$ denote the position vector, r is the magnitude of $\vec{r}$, $\langle ... \rangle$ represents the ensemble average, l_0 and L_0 are the inner and outer scales of the atmospheric turbulence and have units of m.

Being similar to the atmospheric refractive index structure constant C_n^2, the temperature structure constant (C_T^2), absolute humidity structure constant (C_q^2) and the temperature-humidity cross-structure constant (C_{Tq}) can be defined as

$$C_T^2 = \frac{\langle[T(\vec{x}) - T(\vec{x}+\vec{r})]^2\rangle}{r^{2/3}}, l_0 \ll r \ll L_0, \tag{6a}$$

$$C_q^2 = \frac{\langle[q(\vec{x}) - q(\vec{x}+\vec{r})]^2\rangle}{r^{2/3}}, l_0 \ll r \ll L_0, \tag{6b}$$

$$C_{Tq} = \frac{\langle[T(\vec{x}) - T(\vec{x}+\vec{r})][q(\vec{x}) - q(\vec{x}+\vec{r})]\rangle}{r^{2/3}}, l_0 \ll r \ll L_0. \tag{6c}$$

#260823 Received 8 Mar 2016; revised 13 May 2016; accepted 31 May 2016; published 8 Jun 2016

Applying Eqs. (5) and (6) to Eq. (3), the atmospheric refractive index structure constant C_n^2 can be defined in terms of C_T^2 , C_q^2 and C_{Tq}, as follows

$$C_n^2 = A^2 C_T^2 + 2ABC_{Tq} + B^2 C_q^2. \tag{7}$$

3.2. The Bulk C_n^2 model in near-surface layer

According to MOST, the dimensionless function (ξ) is used to express the dynamic near-surface layer property. The ξ value is often referred to simply as the "stability", and is negative in unstable conditions, zero in neutral conditions, and positive in stable conditions, defined as

$$\xi = \frac{zkg(T_* + 0.61Tq_*)}{\vartheta_v u_*^2}, \tag{8}$$

in which z is the height above the sea surface (m), k is the von-Karman constant (0.35), g is the gravitational acceleration, ϑ_v is the virtual potential temperature, T_*, q_* and u_* are the scaling parameters for temperature, absolute humidity and wind speed, respectively.

By using the MOST in near-surface layer, the C_T^2, C_q^2 and C_{Tq} can be expressed in terms of T_* and q_*. The expressions C_T^2, C_q^2 and C_{Tq} are given as follows [33]

$$C_T^2 = T_*^2 z^{-2/3} f_T(\xi), \tag{9a}$$

$$C_q^2 = q_*^2 z^{-2/3} f_q(\xi), \tag{9b}$$

$$C_{Tq} = \gamma_{Tq} T_* q_* z^{-2/3} f_{Tq}(\xi), \tag{9c}$$

where the empirically determined dimensionless functions $f_T(\xi)$, $f_q(\xi)$ and $f_{Tq}(\xi)$ are determined by experiment, Andreas [34] demands $f_T(\xi) = f_q(\xi) = f_{Tq}(\xi)$. γ_{Tq} is the temperature-humidity correlation coefficient. We use a value of 0.5 for $\frac{\Delta T}{\Delta q} \leq 0$, and a value of 0.8 when $\frac{\Delta T}{\Delta q} \geq 0$ in this work, following [34,35]. A typical expression $f_T(\xi)$ is given by Wyngaard [24]

$$f_T(\xi) = \begin{cases} 4.9(1-7\xi)^{-2/3}, \xi \leq 0, \\ 4.9(1+2.75\xi), \xi \geq 0. \end{cases} \tag{10}$$

The scaling parameters for wind speed (u_*), temperature (T_*) and absolute humidity (q_*) within the near-surface are defined as the integrated forms of the empirically determined dimensionless functions $\Psi_U(\xi)$, $\Psi_T(\xi)$ and $\Psi_q(\xi)$ below

$$u_* = kU(z)[ln(\frac{z}{z_{oU}}) - \Psi_U(\xi)]^{-1}, \tag{11a}$$

$$T_* = k[T(z) - T_s][ln(\frac{z}{z_{oT}}) - \Psi_T(\xi)]^{-1}, \tag{11b}$$

$$q_* = k[q(z) - q_s][ln(\frac{z}{z_{oq}}) - \Psi_q(\xi)]^{-1}, \tag{11c}$$

where the functions $U(z)$, $T(z)$ and $q(z)$ are the wind speed, temperature and absolute humidity at height z, respectively. z_{oU} , z_{oT} and z_{oq} are the "roughness lengths" of wind speed, temperature and absolute humidity, respectively. The expression z_{oU} can be parameterized as follows [36]

$$z_{oU} = \frac{\alpha u_*^2}{g} + \frac{0.11v}{u_*}, \tag{12}$$

where v is the kinematic viscosity of air (1.4607×10^{-5} m^2/s), and we have used a value of 0.0185 for α which is determined by experiment [37].

#260823 Received 8 Mar 2016; revised 13 May 2016; accepted 31 May 2016; published 8 Jun 2016

Seeing that the scalar roughness lengths behave quite similarly, the expression $z_{oT} = z_{oq}$ is assumed [38]. The temperature roughness lengths z_{oT} can be parameterized as

$$z_{oT} = R_T \frac{\nu}{u_*}, \tag{13}$$

where R_T is the roughness Reynolds numbers for temperature. R_T is parameterized in terms of the roughness Reynolds number for wind speed, $R_U = z_{oU}\frac{u_*}{\nu}$. The expression R_T can be expressed as

$$R_T = \frac{5.4R_U^{4/3}}{(1.75R_U+1)^2}. \tag{14}$$

Substituting the Eq. (12) and Eq. (14) into the Eq. (13), we obtain the expression for the temperature roughness lengths z_{oT} as follows

$$z_{oT} = \frac{5.4\nu(\frac{\alpha u_*^3}{g\nu}+0.11)^{4/3}}{u_*[1.75(\frac{\alpha u_*^3}{g\nu}+0.11)+1]^2}. \tag{15}$$

In this study, we follow the usual assumption that $\Psi_T(\xi) = \Psi_q(\xi)$ [39,40]. The expression $\Psi_U(\xi)$ and $\Psi_T(\xi)$ are given as follows

$$\Psi_T(\xi) = \begin{cases} 2ln[\frac{1+(1-16\xi)^{1/2}}{2}], \xi \le 0, \\ 1-(1+\frac{2a}{3}\xi)^{3/2} - b(\xi-\frac{c}{d})exp(-d\xi) - \frac{bc}{d}, \xi \ge 0\ ; \end{cases} \tag{16a}$$

$$\Psi_U(\xi) = \begin{cases} 2ln[\frac{1+(1-20\xi)^{1/4}}{2}] + ln[\frac{1+(1-20\xi)^{1/2}}{2}] - 2arctan[(1-20\xi)^{1/4}] + \frac{\pi}{2}, \xi \le 0, \\ -a\xi - b(\xi-\frac{c}{d})exp(-d\xi) - \frac{bc}{d}, \xi \ge 0, \end{cases} \tag{16b}$$

where a = 1, b = $\frac{2}{3}$, c = 5, and d = 0.35.

We can express ξ by solving Eq. (11) for the scaling parameters u_*, T_* and q_*, and combining with Eq. (8). The expression of stability function ξ can be expressed as

$$\xi = \frac{zg(\Delta T + 0.61T\Delta q)[ln(\frac{z}{z_{oU}}) - \Psi_U(\xi)]^2}{\vartheta_v(\Delta U)^2[ln(\frac{z}{z_{oT}}) - \Psi_T(\xi)]}. \tag{17}$$

Therefore, substituting the scaling parameters u_*, T_*, q_* into Eq. (7) and Eq. (9). The expression C_n^2 can be expressed as below

$$C_n^2 = \frac{k^2 f_T(\xi)[A^2(\Delta T)^2 + 2AB\gamma_{Tq}\Delta T\Delta q + B^2(\Delta q)^2]}{z^{2/3}[ln(\frac{z}{z_{oT}}) - \Psi_T(\xi)]^2}, \tag{18}$$

where the operator Δ denotes air-sea difference. Thus, the air-sea difference for temperature, absolute humidity and wind speed (ΔT, Δq, ΔU) are calculated by WRF model outputs. Finally, the functions ξ, $f(\xi)$, Ψ_ξ and C_n^2 are all expressed by ΔT, Δq and ΔU, then C_n^2 can be calculated by solving Eqs. (17) and (18) with an iterative process (see [41] for details).

4. Micro-thermometer

4.1. The principle of micro-thermometer

For visible and near-infrared light, the refractive index fluctuation is mainly caused by temperature fluctuation. The relationship between refractive index structure constant C_n^2 and temperature structure constant C_T^2 is given by [1, 20]

$$C_n^2 = (79\times10^{-6}\frac{P}{T^2})^2 C_T^2, \tag{19}$$

#260823 Received 8 Mar 2016; revised 13 May 2016; accepted 31 May 2016; published 8 Jun 2016

where T is air temperature (K), and P is air pressure (hPa). The process for calculating C_T^2 involves the measurement of the square and average of the temperature difference given by two sensors which are separated by a known distance r in the inertial region. The C_T^2 is defined as the constant of proportionality in the inertial subrange form of the temperature structure function $D_T(r)$. As defined by Obukhov [42], the temperature structure constant (C_T^2) for a Kolmogorov type spectrum is related to the temperature structure function ($D_T(r)$) as below

$$D_T(r) = \langle [T(\vec{x}) - T(\vec{x}+\vec{r})]^2 \rangle, \tag{20a}$$

$$= C_T^2 r^{2/3} \quad for \;\; l_0 \ll r \ll L_0 \; . \tag{20b}$$

The platinum probe has a linear resistance-temperature coefficient, and responds to an increase in atmospheric temperature with an increase in resistance. In our case, the probes used to measure the temperature difference at two points which are horizontally separated by 1.0 m apart. The two probes are legs of a Wheatstone bridge, and the resistance of the probe is very nearly proportional to temperature and thus temperature changes are sensed as an imbalance voltage of the bridge. The micro-thermometer system provides C_T^2 data by measuring mean square temperature fluctuations and thus C_n^2 data can be acquired.

4.2. Brief description of the micro-thermometer measurement

The C_n^2 values measured by micro-thermometer are used to validate the C_n^2 values forecasted by WRF model. A 10 μm diameter, 20 mm long platinum wire is used as micro-thermometer probe which has the frequency response range of 0.05-30 Hz (within the inertial subrange of the atmospheric turbulence spectrum) and the equivalent rms noise is about 0.002 K. The micro-thermometer is placed on the stern stretch out about 5 m above the sea-level, shown in Fig. 2, and the ship drops anchor close to the center grid of simulation domain (17.5°N, 109.5°E).

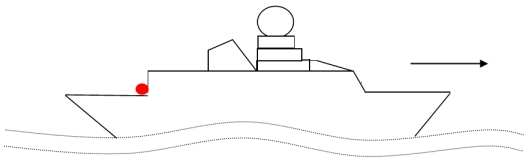

Fig. 2. The measurement ship drops anchor close to the center grid of simulation domain (17.5°N, 109.5°E) over the ocean. The red solid circle represents micro-thermometer location (stretch out about 5 m above sea-level), and the arrow represents the ship prow.

The micro-thermometer measured C_n^2 values are sampled at 4 seconds time interval, while WRF model outputs at 30 minutes time interval owing to the model configuration limitation. The measured values are averaged over the same time interval (30 minutes) to match with the simulated ones for a meaningful comparison. We should note that WRF model outputs are saved as UTC time format while the micro-thermometer values are saved as Local time format (Local time = UTC time + 08:00). WRF outputs and micro-thermometer data available for comparison are listed in Table 3. In addition, the sky conditions from 8 Jul 2014 to 12 Jul 2014 are all in sunny day, while from 13 Jul 2014 to 14 Jul 2014 are in cloudy or overcast day during the maritime experiment. Furthermore, there is wind field perturbation in early days, while it evolves into stabilization soon afterwards. The high pressure ridge transports from Hainan Island to ocean through time, and the experiment area is located in the control of a high pressure system. The atmospheric condition over the ocean near surface is relatively stable in the view of the real meteorological conditions during the experiment.

#260823 Received 8 Mar 2016; revised 13 May 2016; accepted 31 May 2016; published 8 Jun 2016

Table 3. WRF and micro-thermometer data are available for comparison.

Method	Time format	Time interval	Total days	Average time interval
WRF	UTC	30 minutes	5	30 minutes
Micro-thermometer	Local time	4 seconds	5	

Besides, we all know that model error increases through time, so it is fair to expect that a 60-h (3^{rd} day) forecast might have a larger error than a 12-h (1^{st} day) forecast. The model is run on 2 different nights using the procedure described before in order to avoid model error increasing through a long time-series. Each WRF run is initialized with the GFS data which is released at 12:00 UTC of each day before the running date (7 Jul, 2014 and 11 Jul, 2014). All the simulation times are listed in Table 4.

Table 4. WRF simulation times.

Simulation No.	Simulation time	
	Start time	End time
1	2014-07-07-16:00 UTC	2014-07-09-16:00 UTC
2	2014-07-11-16:00 UTC	2014-07-14-16:00 UTC

5. Result

5.1. The diurnal feature comparison of C_n^2 between WRF model and micro-thermometer

The diurnal feature of the near-surface C_n^2 forecasted by WRF model and measured by micro-thermometer over the ocean is shown in Fig. 3. To facilitate direct comparison, measured values are also overlaid in Fig. 3. One can see that the forecasted C_n^2 is consistent with the measured C_n^2 in trend and the order of magnitude in general, and it has the diurnal variation feature of the near-surface optical turbulence over the ocean. The "sharp drop-offs" of C_n^2 during the morning and evening transitions are hardly any visible in this plot. The diurnal variation of the forecasted C_n^2 is relatively stable, while the diurnal variation of measured C_n^2 is obvious. Moreover, the forecasted C_n^2 values almost always correctly capture the order of magnitude which experiences fluctuations of two orders of magnitude, although the forecasted C_n^2 slightly underestimates the measured C_n^2 at times. Note that the discontinuity (Jul 9 to Jul 12) naturally occurs with different simulations, as it is no data assimilation performed.

5.2. Statistical analysis

We evaluate the reliability of C_n^2 forecasted by WRF model using four statistical operators: the BIAS, the root mean square error (RMSE), the bias-corrected RMSE (σ) and the correlation

#260823 Received 8 Mar 2016; revised 13 May 2016; accepted 31 May 2016; published 8 Jun 2016

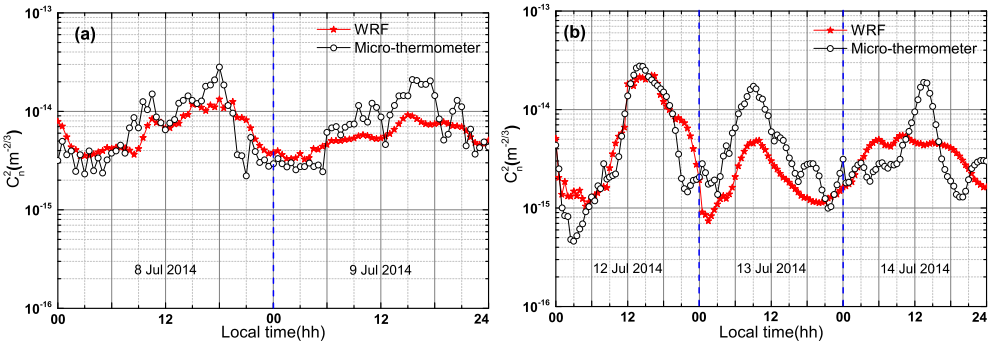

Fig. 3. The diurnal feature comparison of C_n^2 between forecasted by WRF (red solid star) and measured by micro-thermometer (black hollow circle) over the ocean near-surface. (a) Date from Jul 8 to 9, 2014; (b) Date from Jul 12 to 14, 2014, respectively.

coefficient (R_{xy}). The expression BIAS, RMSE, σ, R_{xy} are defined as

$$BIAS = \sum_{i=0}^{N} \frac{\Delta_i}{N}, \tag{21a}$$

$$RMSE = \sqrt{\sum_{i=0}^{N} \frac{(\Delta_i)^2}{N}}, \tag{21b}$$

$$\sigma = \sqrt{RMSE^2 - BIAS^2}, \tag{21c}$$

$$R_{xy} = \frac{\sum_{i=0}^{N}(X_i - \overline{X}_i)(Y_i - \overline{Y}_i)}{\sqrt{\sum_{i=0}^{N}(X_i - \overline{X}_i)^2 \sum_{i=0}^{N}(Y_i - \overline{Y}_i)^2}}, \tag{21d}$$

with $\Delta_i = Y_i - X_i$ where X_i is the individual C_n^2 value measured by the micro-thermometer, Y_i the individual C_n^2 value forecasted by WRF model at the same time and N is the number of times for which a couple (X_i,Y_i) is available. $\overline{X}_i$ and $\overline{Y}_i$ represent the average value of measured and forecasted parameters.

The correlation of C_n^2 between forecasted by WRF model and measured by micro-thermometer is shown in Fig. 4, and the values of BIAS, RMSE, σ and R_{xy} for near-surface C_n^2 over the ocean are labeled in Fig. 4. One can see that the forecasted C_n^2 agrees with the C_n^2 measured by micro-thermometer overall. The values of BIAS, RMSE and σ are very small, while the R_{xy} is high relatively. Hence, the near-surface C_n^2 values forecasted by WRF model over the ocean are satisfactory.

The histograms and cumulative distributions of overall $\log_{10}(C_n^2)$ forecasted by WRF model and measured by micro-thermometer is shown in Fig. 5. Note that we use the $\log_{10}(C_n^2)$ to replace the C_n^2 for the histograms and cumulative distribution plot readable. It is apparent that the shape of the cumulative distribution of forecasted $\log_{10}(C_n^2)$ is very similar to the measured $\log_{10}(C_n^2)$. From the cumulative distribution, we can extract the mean and the median. The mean (-14.40 vs -14.34) and median (-14.36 vs -14.42) values of $\log_{10}(C_n^2)$ between forecasted by WRF model and measured by micro-thermometer are close to each other, showing again a good coherence between forecasted C_n^2 and measured C_n^2. Consequently, we can confirm that the simulated C_n^2 values in this method are practical overall.

#260823 Received 8 Mar 2016; revised 13 May 2016; accepted 31 May 2016; published 8 Jun 2016

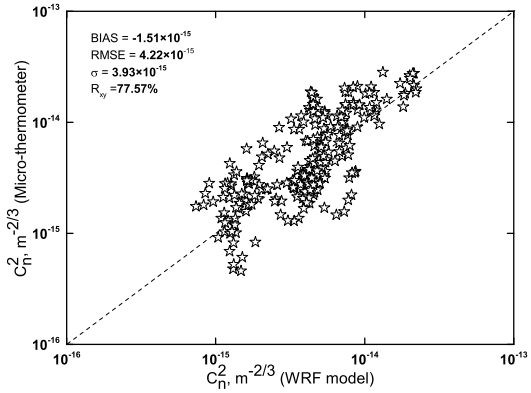

Fig. 4. The correlation of near-surface C_n^2 between forecasted by WRF model (abscissa) and measured by micro-thermometer (ordinate) over the ocean. Each point represents an average of 30 minutes (240 total points).

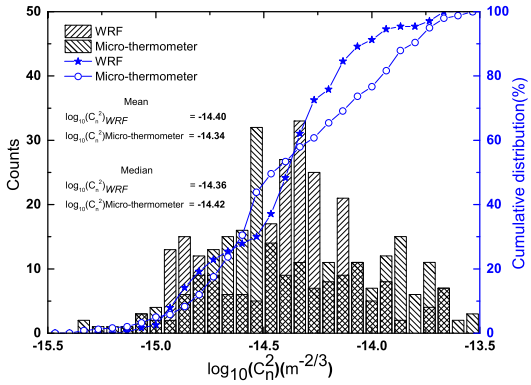

Fig. 5. The histograms (black histogram, left scale) and cumulative distributions (blue symbol curves, right scale) of overall $\log_{10}(C_n^2)$ forecasted by WRF model and measured by micro-thermometer over the ocean near-surface (240 total points).

6. Discussion

In Section 5, we have seen the forecasted C_n^2 is well consistent with the measured C_n^2 in trend and magnitude as a whole, but the forecasted C_n^2 slightly underestimates the measured C_n^2 at times. Here we discuss the possible causes of the deviation and the improvements which will be presented in advance.

(1) In reality, there exists intermittent turbulence or large uncertainties that trigger turbulence so that the value of C_n^2 measured by micro-thermometer is not necessarily very small [1]. Moreover, the C_n^2 value measured by micro-thermometer could be considered as the "point" measurement at a limited domain, while the C_n^2 value forecasted by WRF model coupled with Bulk model should be considered as the statistical average value which is a simplify process of various influencing factor to atmospheric turbulence at 3 km horizontal grid resolution for the center of simulation domain. As far as the impact of the body of a measurement ship to the micro-thermometer value is concerned.

(2) The empirically determined dimensionless functions $f(\xi)$ and $\Psi(\xi)$ which Bulk method depends upon have been determined with greater certainty in unstable conditions than in stable

#260823 Received 8 Mar 2016; revised 13 May 2016; accepted 31 May 2016; published 8 Jun 2016

conditions [43]. The dynamic characteristics of the calculated C_n^2 with Bulk model in unstable surface layer are better than that in stable surface layer in general. The ocean near-surface conditions are more complex than other category of underlying surface relatively, and the measurement height or the height where C_n^2 value was calculated with the method of Bulk model implement in a WRF model may be above the constant flux layer in a region where MOST is not valid when the ocean surface layer can become very thin in very stable conditions. In the future, we will do more sufficient field experiments to gain a more precise understanding the performances of the model under not perfect conditions (for example lack of homogeneity or different conditions of the ocean) and use this understanding to improve current Bulk model for estimating C_n^2.

(3) The surface heterogeneity has a much greater impact on atmospheric turbulence in stable conditions, especially in offshore flow [44]. In this study, the simulation area is in a coastal ocean region where the atmospheric turbulence is impacted by the surroundings greatly and MOST will be invalid if the dynamic atmospheric properties depend upon surface characteristics. It is fair to expect that the C_n^2 forecasted by WRF model using Bulk model will perform better in the open ocean where the atmospheric turbulence is impacted by the surroundings slightly.

(4) In this paper, the lack of measured routine meteorological data which is used to be compared with WRF model is a shortcoming. The functions $f(\xi)$ and $\Psi(\xi)$ used here are the empirical form, and they are probably not appropriate for real ocean surface condition at times. In the future, improvements are expected from WRF model better horizontal grid resolution and outputs time interval, as well as the quite appropriate form of functions $f(\xi)$ and $\Psi(\xi)$ would be adopted.

7. Conclusion

In this paper, a method that WRF model coupled with Bulk model has been able to forecast routine meteorological parameters (such as temperature, relative humidity, pressure, wind speed, etc.), but also the C_n^2 values over the ocean near-surface. It is found that this method almost always captures the correct order of magnitude for C_n^2, which experiences fluctuations of two orders of magnitude in view of the comparison between C_n^2 forecasted by WRF model and C_n^2 measured by micro-thermometer. The forecasted C_n^2 is well consistent with the measured C_n^2 in trend and the orders of magnitude, as well as the values of the bias, the RMSE and the σ for the C_n^2 are very small and the correlation coefficient is up to 77.57%. Therefore, we conclude that WRF model coupled with Bulk model performances in reconstructing the C_n^2 time series above the ocean near-surface is satisfactory. In future work, we will do more sufficient field experiments to gain a better understanding of how C_n^2 behaves with different ocean atmosphere conditions and use this understanding to improve current Bulk model for estimating C_n^2. Furthermore, the forms of functions $f(\xi)$ and $\Psi(\xi)$ are very important to the accuracy of calculating C_n^2 and the quite appropriate form of functions $f(\xi)$ and $\Psi(\xi)$ would be adopted in next work.

The result of this study guarantees a concrete practical advantage from the implementation of any potential optical engineering fields where the instruments are difficult to use and it provides the assistance for the equipment of laser atmospheric transmission over the ocean near-surface.

Acknowledgments

We sincerely acknowledge the reviewers and the editor for their valuable comments and suggestions. We also thank the NCAR and the NCEP for accessing to their initialized meteorological dataset. This work is supported by the National Natural Science Foundation of China (NSFC, Grant Nos.41275020; 41576185).

#260823 Received 8 Mar 2016; revised 13 May 2016; accepted 31 May 2016; published 8 Jun 2016